RAZA: A Rapid 3D z-crossings algorithm to segment electron tomograms and extract organelles and macromolecules

Rubbiya A. Ali[a], Ahmed M. Mehdi[b,f], Rosalba Rothnagel[a], Nicholas A. Hamilton[a], Christoph Gerle[c,d], Michael J. Landsberg[a,e], Ben Hankamer[a,*]

[a] Institute for Molecular Bioscience, The University of Queensland, Brisbane, QLD, Australia
[b] Translational Research Institute, University of Queensland Diamantina Institute, Brisbane, QLD, Australia
[c] Picobiology Institute, Department of Life Science, Graduate School of Life Science, University of Hyogo, Kamigori, Japan
[d] Core Research for Evolutional Science and Technology, Japan Science and Technology Agency, Kawaguchi, Japan
[e] School of Chemistry and Molecular Biosciences, The University of Queensland, Brisbane, QLD, Australia
[f] Department of Electrical Engineering, University of Engineering and Technology, Lahore, Punjab, Pakistan

ARTICLE INFO

ABSTRACT

Resolving the 3D architecture of cells to atomic resolution is one of the most ambitious challenges of cellular and structural biology. Central to this process is the ability to automate tomogram segmentation to identify sub-cellular components, facilitate molecular docking and annotate detected objects with associated metadata. Here we demonstrate that RAZA (Rapid 3D z-crossings algorithm) provides a robust, accurate, intuitive, fast, and generally applicable segmentation algorithm capable of detecting organelles, membranes, macromolecular assemblies and extrinsic membrane protein domains. RAZA defines each continuous contour within a tomogram as a discrete object and extracts a set of 3D structural fingerprints (major, middle and minor axes, surface area and volume), enabling selective, semi-automated segmentation and object extraction. RAZA takes advantage of the fact that the underlying algorithm is a true 3D edge detector, allowing the axes of a detected object to be defined, independent of its random orientation within a cellular tomogram. The selectivity of object segmentation and extraction can be controlled by specifying a user-defined detection tolerance threshold for each fingerprint parameter, within which segmented objects must fall and/or by altering the number of search parameters, to define morphologically similar structures. We demonstrate the capability of RAZA to selectively extract subgroups of organelles (mitochondria) and macromolecular assemblies (ribosomes) from cellular tomograms. Furthermore, the ability of RAZA to define objects and their contours, provides a basis for molecular docking and rapid tomogram annotation.

1. Introduction

Resolving the 3D architecture of cells at an atomic scale is one of the most ambitious challenges of cellular and structural biology, and is accompanied by the promise of delivering unprecedented insight into the complex and dynamic interplay between organelles, subcellular structures, macromolecular assemblies and biomolecules. Currently no single structural technique can achieve this aim, but the use of a set of biophysical techniques spanning the atomic to micron resolution range (e.g. optical microscopy, cellular and single particle electron tomography, bio-molecular NMR, X-ray and electron crystallography) offers the potential to yield 'pseudo-atomic' resolution 3D cellular atlases based on nested, multiscale datasets (Alber et al., 2008). Electron tomography (ET) has benefited from recent significant improvements in

sample preparation (Pantelic et al., 2014), instrumentation (Kuhlbrandt, 2014; Pantelic et al., 2014; Ramachandra et al., 2014; Villa et al., 2013), imaging (McMullan et al., 2014), data capture and image processing and can now routinely deliver information on cellular structures in the 2–5 nm resolution range. These advances now increasingly allow structural biologists to resolve not only organelle and membrane structures, but cytosolic macromolecular assemblies, cellular motors and the extrinsic densities of large membrane proteins embedded in native membranes in unprecedented detail (Daum et al., 2010; Engel et al., 2015). Phase plate technology (Asano et al., 2015; Danev et al., 2014) lessen the detrimental effects of the contrast transfer function by offering the capability to enhance contrast close to focus, to improve the visualization of macromolecular assemblies and ordered subcellular structures in their native environment. For repeated

---

subcellular or molecular structures, improved *in situ* structures can be obtained by applying 3D alignment and averaging routines, through single particle tomography (Castano-Diez et al., 2012; Galaz-Montoya et al., 2015; Hrabe et al., 2012; Nicastro et al., 2006). Finally, using cryo-focused ion beam (cryo-FIB) milling it is now possible to resolve the ultrastructure of subcellular volumes to ~ 4 nm resolution in vitreous ice (Engel et al., 2015) in a relatively high throughput manner.

Given these rapid technological advances both the volume and resolution of tomographic data is rapidly increasing, and with it the need for reliable automated tomogram segmentation procedures capable of detecting organelles and membranes (Cardenes et al., 2017; Martinez-Sanchez et al., 2011; Martinez-Sanchez et al., 2014; Yu et al., 2008), as well as macromolecular assemblies (Comolli et al., 2009) and extrinsic membrane protein domains. A range of noise reduction techniques and segmentation algorithms have been reported for this purpose. Noise reduction techniques include wavelet transforms (Reichel et al., 2001), median filters (Sandberg, 2007; van der Heide et al., 2007), bilateral filters (Jiang et al., 2003; Pantelic et al., 2006), anisotropic (Fernandez, 2009; Fernandez and Carrascosa, 2010; Fernandez et al., 2008) and non-anisotropic diffusion filters (Volkmann, 2010; Yamashita et al., 2007). Segmentation algorithms include drawing and interpolation tools (Alber et al., 2008; Noske et al., 2008), thresholding algorithms (John, 1986; Shapiro and Linda, 2002), ridge detectors (Cardenes et al., 2017) gradient-based edge detectors (Gonzalez 2002a,b; Prewitt, 1970; Roberts, 1963), snake algorithms (Kang et al., 2015; Kass et al., 1988), watershed transforms (Adiga et al., 2004; Roerdink and Meijster, 2001; Sijbers et al., 1997; Volkmann, 2010), bilateral edge filters (Gonzalez 2002a,b; Marr and Hildreth, 1980; Pantelic et al., 2007), Laplacian of Gaussian filters (Marr and Hildreth, 1980), fast marching methods (Bajaj et al., 2003; Baker et al., 2006), the 3D recursive filter (Monga et al., 1991; Yu and Bajaj, 2005), template matching techniques (Comolli et al., 2009; Frangakis et al., 2002; Lebbink et al., 2007), correlation approaches (Zhu et al., 2003) and machine learning approaches (Luengo et al., 2017; Mallick et al., 2004; Moussavi et al., 2010). These tools along with the advantages and drawbacks of each are reviewed more comprehensively elsewhere (Ali, 2016).

Many of the above segmentation techniques operate as 2D or pseudo 3D algorithms (Garduno et al., 2008; John, 1986; Prewitt, 1970; Marr and Hildreth, 1980; Monga et al., 1991; Pantelic et al., 2007; Roberts, 1963; Tomasi and Manduchi, 1998; Woolford et al., 2007) rather than true 3D algorithms (Ali, 2016; Ali et al., 2012) which are theoretically more robust, sensitive and accurate. This is illustrated for a $3 \times 3 \times 3$ voxel 3D kernel in which the central focal pixel focused on an edge, can test 26-way connectivity (i.e. $3 \times 3 \times 3$ voxels = 27 voxels, minus the focal pixel). In contrast a 3x3 pixel 2D kernel only analyses 8-pixel connectivity. Consequently, compared to 2D kernels, 3D kernels can theoretically support improved edge extraction, increasing operational robustness, sensitivity and accuracy.

Automated tomogram segmentation algorithms should ideally also be intuitive (i.e. few parameters to optimize), fast (e.g. > 100× faster than manual segmentation (Ali, 2016) generally applicable and selective. 'Generally applicable' is defined as the ability to segment a range of 3D dataset types (e.g. cryo-ET, FIB-SEM) as well as the multitude of organelles, macromolecules and extrinsic membrane proteins within cells. As all resolved objects have edges, edge detection algorithms, as opposed to template matching algorithms for example, are well suited to provide such general approaches. Selectivity is defined as the ability to specifically identify and extract a set of target object (e.g. ribosomes) from the multitude of contoured 3D objects in a fully segmented tomogram. Such selectivity can be supported by defining contours as geometric objects with defined dimensions which provide structural fingerprints, as opposed to simply demarcating objects with pixels contours, as is the case of most of the above algorithms.

Here, we present RAZA (<u>Ra</u>pid 3D <u>z</u>-crossings <u>A</u>lgorithm) a 3D edge detection algorithm that was designed to meet the above criteria (robust, sensitive, accurate, intuitive, fast, generally applicable and selective). It integrates a Laplacian of Gaussian (LoG) kernel, with arbitrary z-crossings and structural finger printing algorithms and is able to segment low signal-to-noise ratio (SNR) data typical of 3D reconstructed volumes obtained from electron tomography of resin embedded and vitrified samples, as well as 3D volumes obtained using serial block face-scanning electron microscopy (Starborg et al., 2013) or focused ion beam-scanning electron microscopy (Kizilyaprak et al., 2015). The 3D LoG operator simultaneously denoises and detects edges in the tomographic volume. Edges are defined as regions exhibiting a 'significant change' in voxel intensity compared to their surroundings. This change in intensity enables the segmentation of all structurally resolved objects within a tomographic volume, independent of size, shape or relative orientation (Fig. S1) at speeds typically 4000× greater than can be achieved by manual segmentation. The fit of these contours can be optimized through the adjustment of the z-crossings value. RAZA defines each continuous contour within a tomographic volume as a discrete geometric object, as opposed to conducting simple pixel based edge delineation. The importance of this is that each geometrically defined object yields a set of 'structural fingerprint' parameters (major, middle and minor axes, surface area and volume), which enable selective, object identification, segmentation and the extraction of organelles (Fig. 2), macromolecules (Fig. 4), membranes (Fig. 3) and extrinsic membrane domains (Fig. 3) from both plastic embedded (Fig. 6), cryo-ET (Fig. 7) and FIB-SEM dataset (Fig. S7).

2. Methods

2.1. Algorithm design

RAZA combines two computational components; 1. denoising/edge detection and 2. object selection. RAZA first applies a Gaussian denoising filter coupled with Laplacian filtration to generate a second derivative image volume of the contoured objects (see Fig. 1). In so doing RAZA conducts autonomous, non-contextual segmentation which does not require prior knowledge of the objects.

3. 3D Laplacian of Gaussian (LoG)

The first step of RAZA requires the generation of a Laplacian of Gaussian (LoG) volume. The Gaussian function (Gonzalez 2002a,b) smooths the focal voxel based on the sigma (σ) value which defines the radius of its 3D kernel. In three dimensions, the Gaussian function of a volume with continuous voxels (x, y, z) is defined as:

$$G(x,y,z) = \frac{1}{2\pi\sigma^2} e^{\frac{-(x^2+y^2+z^2)}{2\sigma^2}} \tag{1}$$

where x, y and z are coordinates of the focal voxel and σ determines the radius of the Gaussian (G) kernel. Similarly, the Laplacian (L) yields the second-order derivative of a 3D object, which is defined as:

$$L(x,y,z) = \frac{\partial^2 I(x,y,z)}{\partial x^2} + \frac{\partial^2 I(x,y,z)}{\partial y^2} + \frac{\partial^2 I(x,y,z)}{\partial z^2} \tag{2}$$

where, $L(x,y,z)$ refers to the Laplacian function, defined as the sum of the second derivative of the test volume relative to x, y and z respectively. Finally, by applying the Laplacian (Eq. (2)) onto a Gaussian-filtered volume (Eq. (1)), the equation becomes:

$$LoG(x,y,z) = C\left(\frac{x^2}{\sigma_x^4} - \frac{1}{\sigma_x^2} + \frac{y^2}{\sigma_y^4} - \frac{1}{\sigma_y^2} + \frac{z^2}{\sigma_z^4} - \frac{1}{\sigma_z^2}\right) e^{-\frac{x^2}{2\sigma_x^2} - \frac{y^2}{2\sigma_y^2} - \frac{z^2}{2\sigma_z^2}} \tag{3}$$

where C is an arbitrary real constant (set to 1 in the source code). The use of a small value of σ results in a small Gaussian kernel radius. This is best suited to preserve fine details but does not give the same degree of smoothing as a larger σ value, which can assist with the detection of larger objects. The *LoG* operation yields calculated voxel intensities, which range from negative to positive or vice versa (Fig. S2).
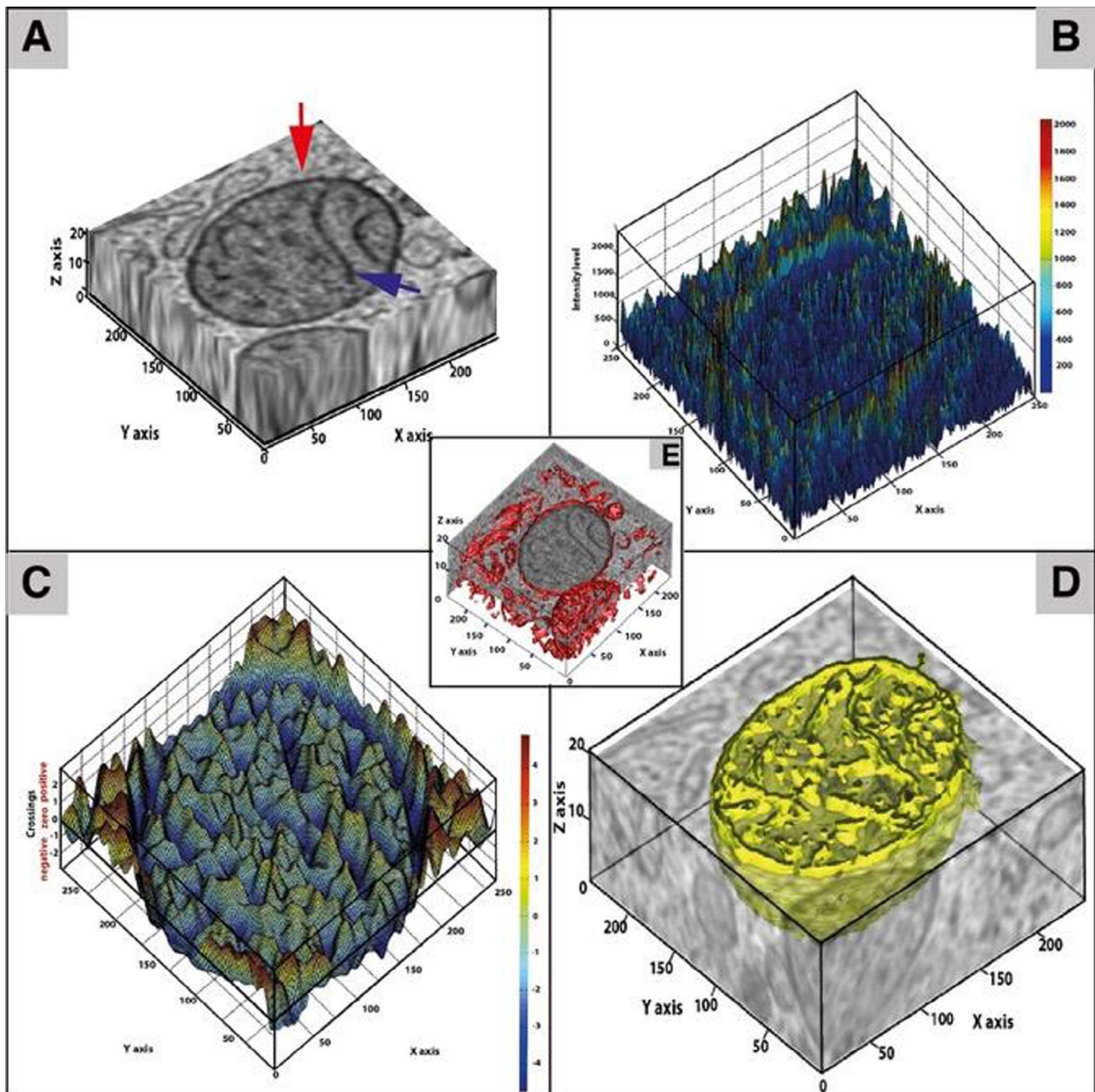
Fig. 1. RAZA filter concept. A) The raw subvolume containing a mitochondrion of an insulin-secreting pancreatic beta cell. B) The first-order derivative of the Gaussian filtered tomogram. The *X* and *Y*-axes are the *X-Y* tomogram axes of panel A. The *Z*-axis represents the range of first-order derivatives of the greyscale intensity values of Fig. 2A, which are color-coded from, blue (0) to red (2000) and peak around the edges. C) The second-order derivative of the Gaussian filtered tomogram. The *X* and *Y*-axes are the *X-Y* tomogram axes. The *Z*-axis represents the second-order derivative values color coded from positive (red) to negative (blue). Yellow coloring indicates zero crossings. D) The rendered tomogram (z-crossings value = 1.5 and σ = 0.49). z-crossings values were traced for the full tomogram and unwanted contours (outside mitochondrion region) were deleted, leaving the rendered mitochondrion. (E) Z-crossed volume excluding the mitochondrion region, which can be extracted manually as in D or in an automated manner using the structural finger print functionality described below.

3.1. Arbitrary z-crossings concept in 3D

A zero-crossing is defined as a point where the sign of the intensity values of a LoG volume changes from positive to negative or negative to positive. This identifies the most rapid change in discontinuity of the original volume. Mathematically, an edge can be defined as a region of increased discontinuity and so in the zero-crossings scenario, where the output LoG volume contains an intensity value equal to '0', it marks this as a point on an edge. In 2007 (Woolford et al., 2007) showed that modifying a 2D zero crossings algorithm to instead incorporate an

'arbitrary z-crossing' value can provide significant benefits. This is because LoG filtered volumes do not only contain zero but also negative and positive intensity values that can be selected to trace an edge voxel. To determine whether non-zero LoG values belong to a true edge or not, each voxel is scanned by RAZA to define: (1) whether its intensity is negative, zero or positive; and (2) whether any of its neighbor voxels in 3D (i.e. the 26 voxels surrounding the central voxel in a $3 \times 3 \times 3 = 27$ voxel box) has a z-crossings value of opposite sign. If the above conditions are fulfilled the voxel will be considered a 'true' edge voxel. It can be understood that a positive choice for the z-crossings value favors
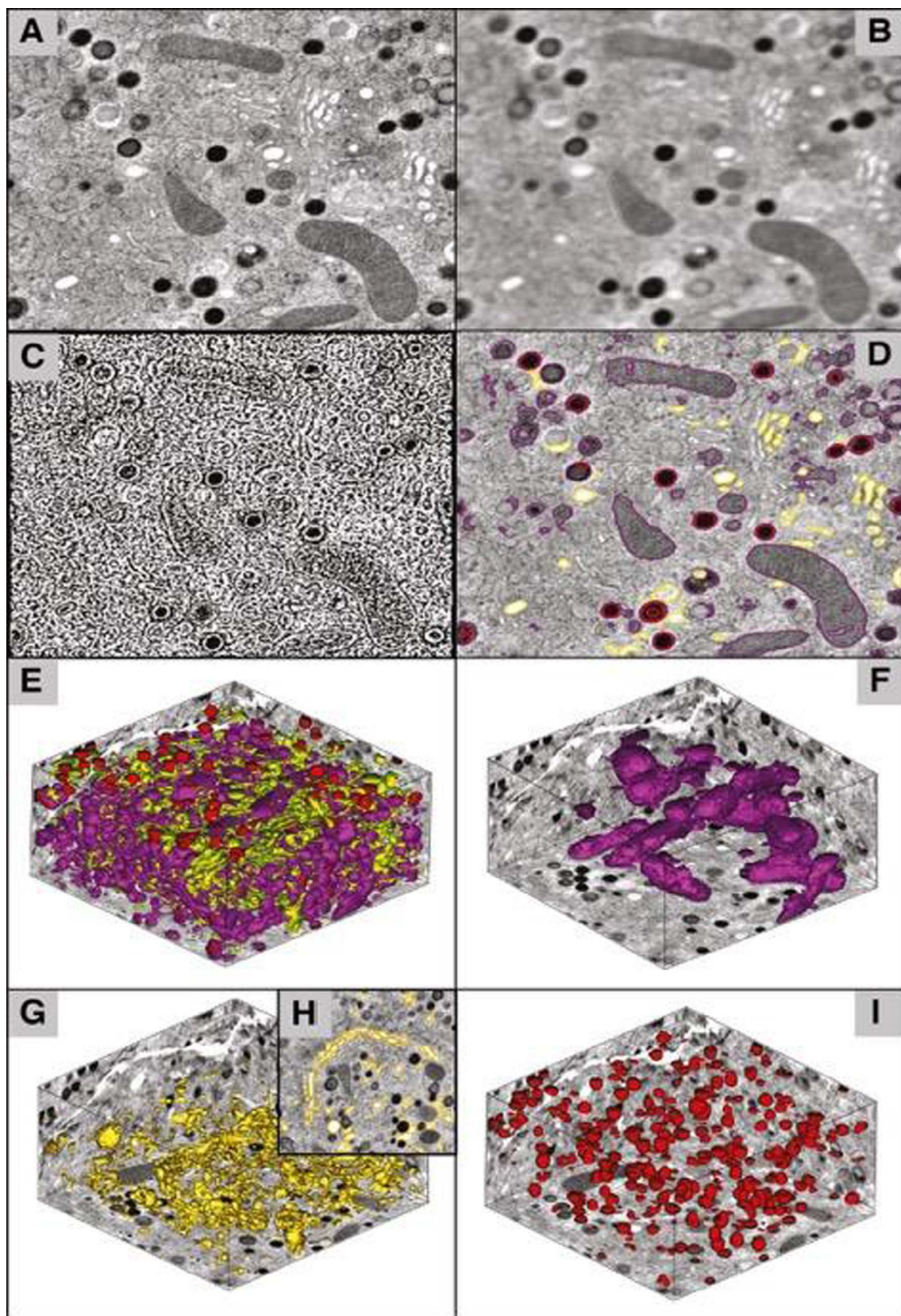
Fig. 2. Application of RAZA filter to a cellular tomogram. (A) Tomographic volumes that encompassed key compartments involved in insulin production and release by beta cells. (B) Gaussian filtered tomogram shown in A. (C) Application of the Laplacian of Gaussian (LoG) and zero crossing algorithms to the tomogram shown in A. (D) The contours detected by RAZA filter overlaid on the 2D tomographic view shown in A: White objects (mainly Golgi regions – a complete and more clear Golgi region with contours detected by RAZA is shown in H) contoured in yellow (z-crossings value = 1170 and σ = 0.58), light gray objects (mainly mitochondria) contoured in purple (z-crossings value = −1 and σ = 0.49), dark gray objects and dark circular objects (mature (insulin) granules) contoured in red (z-crossings value = −2405 and σ = 0.49). (E) All the contours represented in the 3D tomographic view. (F, G and I) show 3D surface views of all the white, gray and dark gray objects respectively.
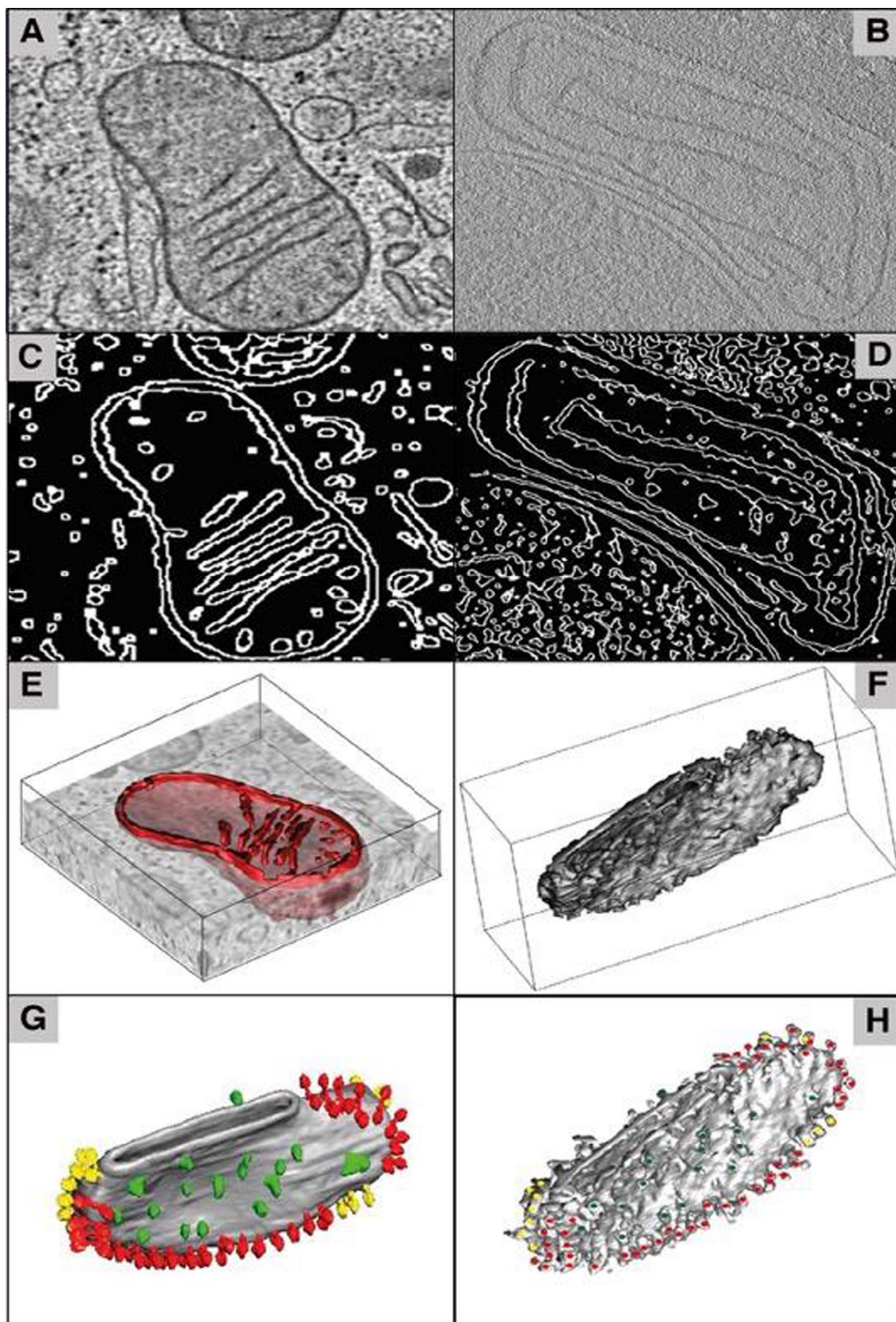
Fig. 3. Detection of membranes and membrane proteins imaged under negative stain (chemically fixed) and cryo-conditions. (A) Negatively stained (fixed) tomographic slice of a mitochondria and its cristae from a pancreatic beta cell. (B) A cryo-tomographic slice containing a membrane (crista vesicle from *P. anserina*). (C) Application of RAZA filter using z-crossings = 10 and σ = 0.52 showing the detected mitochondrial and cristae boundaries shown in A. (D) Application of RAZA filter using σ = 0.49 and z-crossings = 10 showing the detected cristae boundaries shown in B. (E) 3D surface view of segmented mitochondria (shown in A) obtained by RAZA after post-processing to delete unwanted edges. (F) 3D surface view of a segmented mitochondrial crista (shown in B) obtained by RAZA. (G) 3D surface of crista membrane. ATPase complexes observed protruding from the membrane are color-coded as in (Davies et al., 2011). (H) An enlarged representation of the 3D surface view shown in F with the ATPase complexes detected by RAZA, manually color-coded according to G to facilitate comparison.
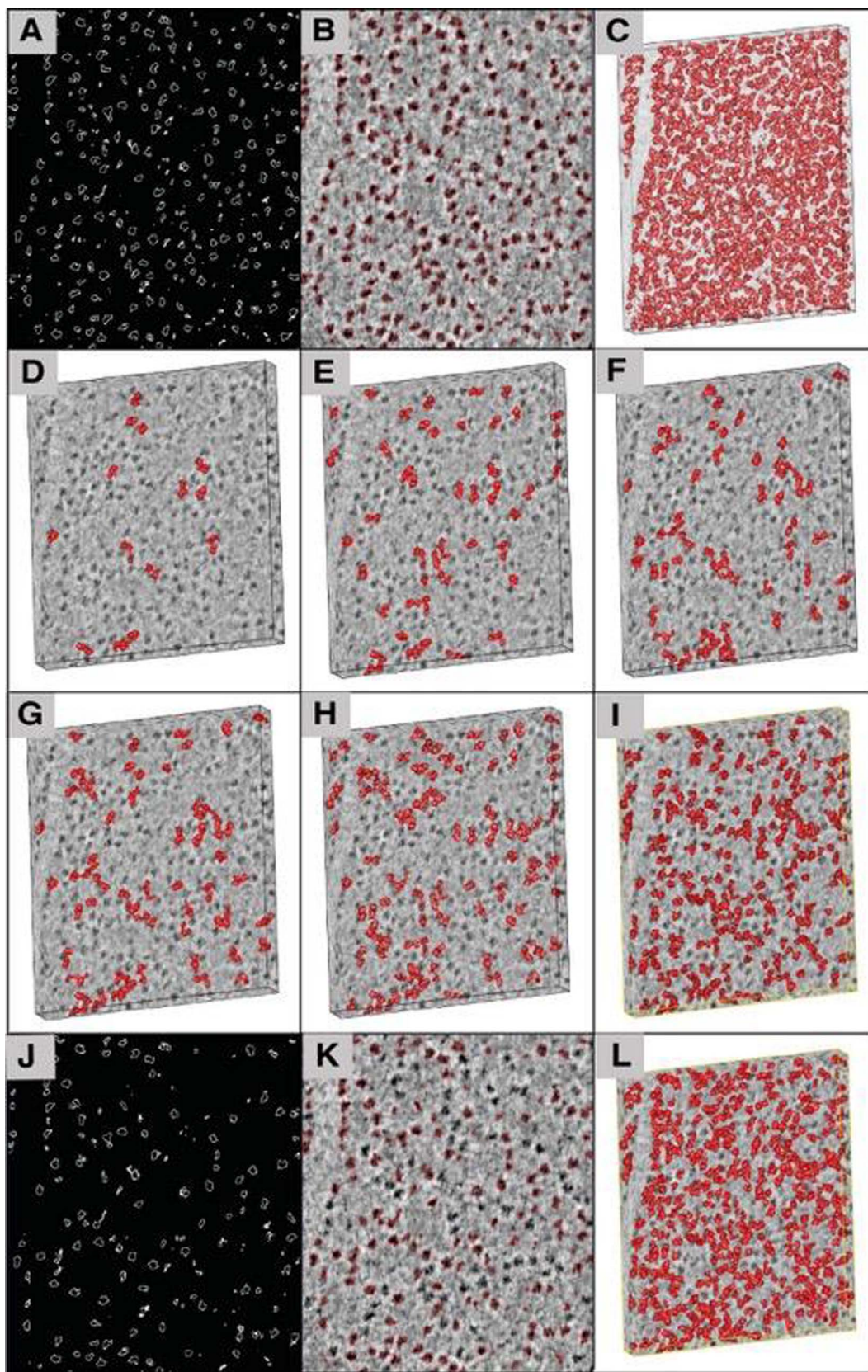
Fig. 4. Detection of ribosome like macromolecular assemblies from an electron tomographic subvolume. Macromolecular assemblies were contoured using RAZA settings of z-crossings = −1 and σ = 0.8. (A) Application of RAZA using basic settings (z-crossings = −1 and σ = 0.8 without using structural fingerprints). (B) Detected contours (red) overlaid on input gray scale tomogram. (C) 3D surface rendered views of the detected objects shown in B. (D) 3D surface rendered views of the detected objects at a ± 20% threshold setting using all three axes, surface area and volume (high stringent) as search parameter. (E) 3D surface rendered views at a ± 20% threshold setting for only the 3D axes. (F) 3D surface rendered views of the detected objects at a ± 20% threshold setting for only the 3D volume. (G) Application of RAZA at a ± 20% threshold setting for the surface area. (H) 3D surface rendered views of the detected objects using major axis. (I) Application of RAZA at ± 20% threshold setting when only the minor axis threshold. (J) Application of RAZA at ± 80% threshold setting based on only the minor axis settings. (K) Contour overlaid on gray scale input tomogram (L) 3D surface rendered views of detected objects shown in K.
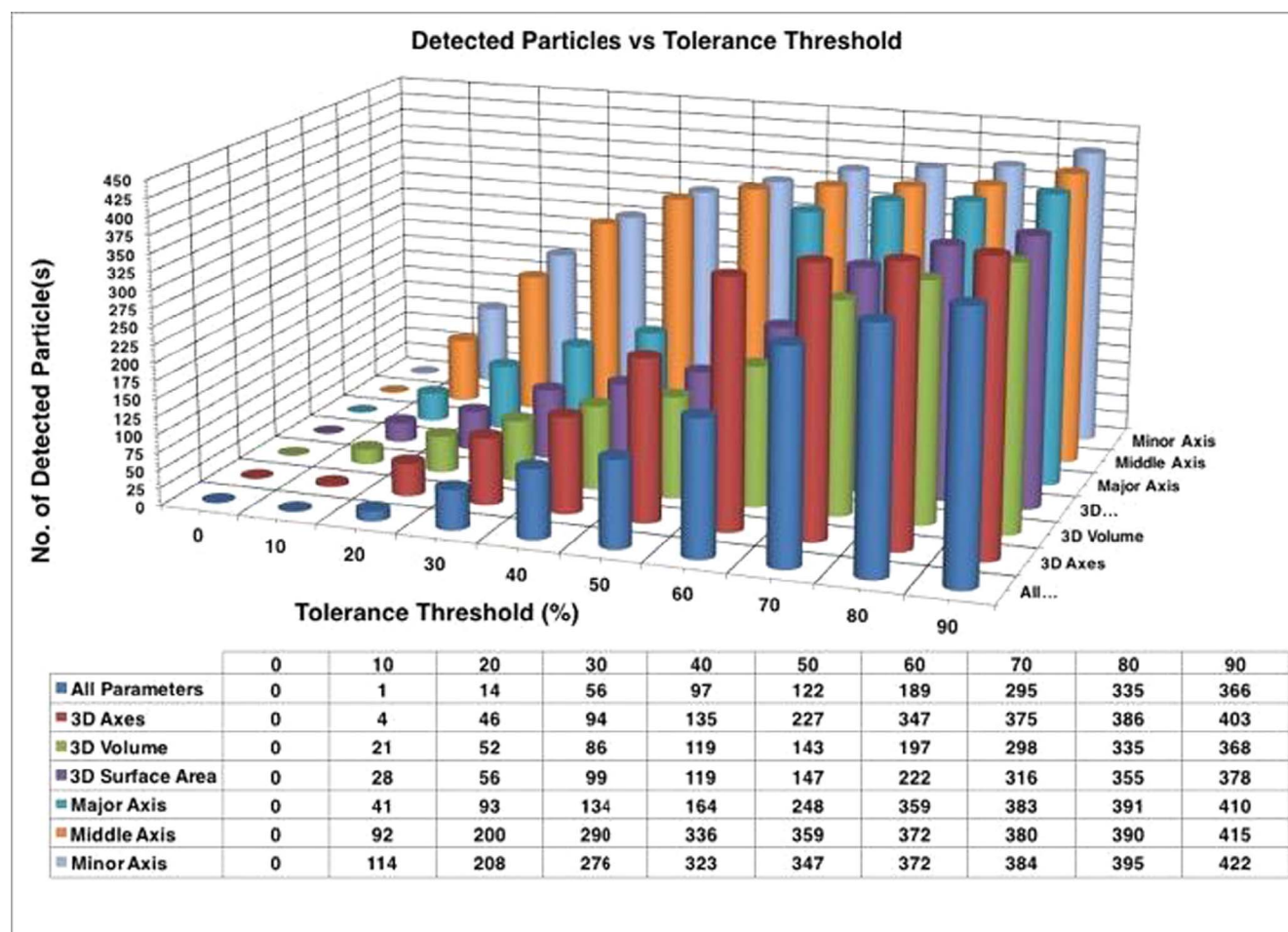
Fig. 5. Finger print parameter based ribosome-like objects detection in a tomographic volume. The tomographic volume used for this analysis is shown in Fig. 4. The 0% Tolerance threshold value corresponds to the average value calculated for each parameter based on 10 selected ribosomes. The rising tolerance threshold (%) values correspond to the average values calculated ± the indicated percentage of this average (e.g. 20%). Using all 5 fingerprint parameters (All parameters: 3 axes, Surface area and Volume) results in the most stringent selection. Alternatively, all three axes (3D axes), single axes (e.g. Major. middle or minor), 3D Surface area or volume can be chosen to search the data set (see also Fig. S1). The particle detection rates are shown as a function of the increasing tolerance thresholds based on seven different search parameter combinations: major, middle and minor axis lengths (separately), 3D surface area, 3D volume, all three axis lengths simultaneously, and all five individual parameters applied individually.

the tracing of lighter objects on a darker background (Fig. S2 A and B) and that a negative choice of z-crossings, as shown in Fig. S2 E and F, favors tracing of darker objects on light backgrounds.

The process always generates a closed contour. This greatly simplifies the extraction of quantitative properties for segmented objects. For example, within a complete 3D contour, the '*major axis*', which is defined as the vector connecting two voxels separated by the greatest distance that form part of the object contour, can be readily identified. After the identification of the major axis, the *middle* axis is defined as the maximum distance between two voxels, with the additional constraint that it be perpendicular to the major axis vector. The *minor* axis is mutually orthogonal to the middle and major axis vectors, its length defined by the contour boundary. These three axes provide the height, length and width of the object. Their point of intersect is defined as the object *centroid*, which can be used for sub-volume extraction. Importantly, using a true 3D filter such as RAZA, the object axes are not restrained to the x, y, z reference axes of the tomogram. This is important as it allows the major, middle and minor axes to be identified irrespective of the orientation of the object in the tomogram. Step-by-step instructions for the extraction of sub-volumes along with object specific x, y, z axis information can be found in Supplementary Material I (Fig. S5).

From the continuous contour of an identified object the '*surface area*' and '*volume*' can be calculated. The *surface area*, is calculated from

the length of each contour within each 2D slice (in the *xy* plane) of a 3D volume. It then sums the lengths of all the contours in the Z-direction. The *volume* of the object, is calculated from the total number of voxels enclosed within the contour including edge voxels.

Collectively these five parameters (three axes, the surface area and volume) provide an object specific '*3D structural finger print*'. This allows the user to define and select a discrete class of subcellular objects (e.g. ribosomes or organelles of particular interest) for segmentation and extraction (Fig. S1).

3.2. Implementation and availability

RAZA was programmed in C using IMOD image processing libraries (Kremer et al., 1996). The compiled source code for RAZA was tested on CentOS 6. RAZA software (including source files) is freely available on request for academic use, together with the installation instructions and user manual (Supplementary Material II) .

3.3. Electron tomographic data collection

The performance of RAZA was evaluated using seven test datasets acquired by electron tomographic methods, representing both vitrified and resin-embedded samples.
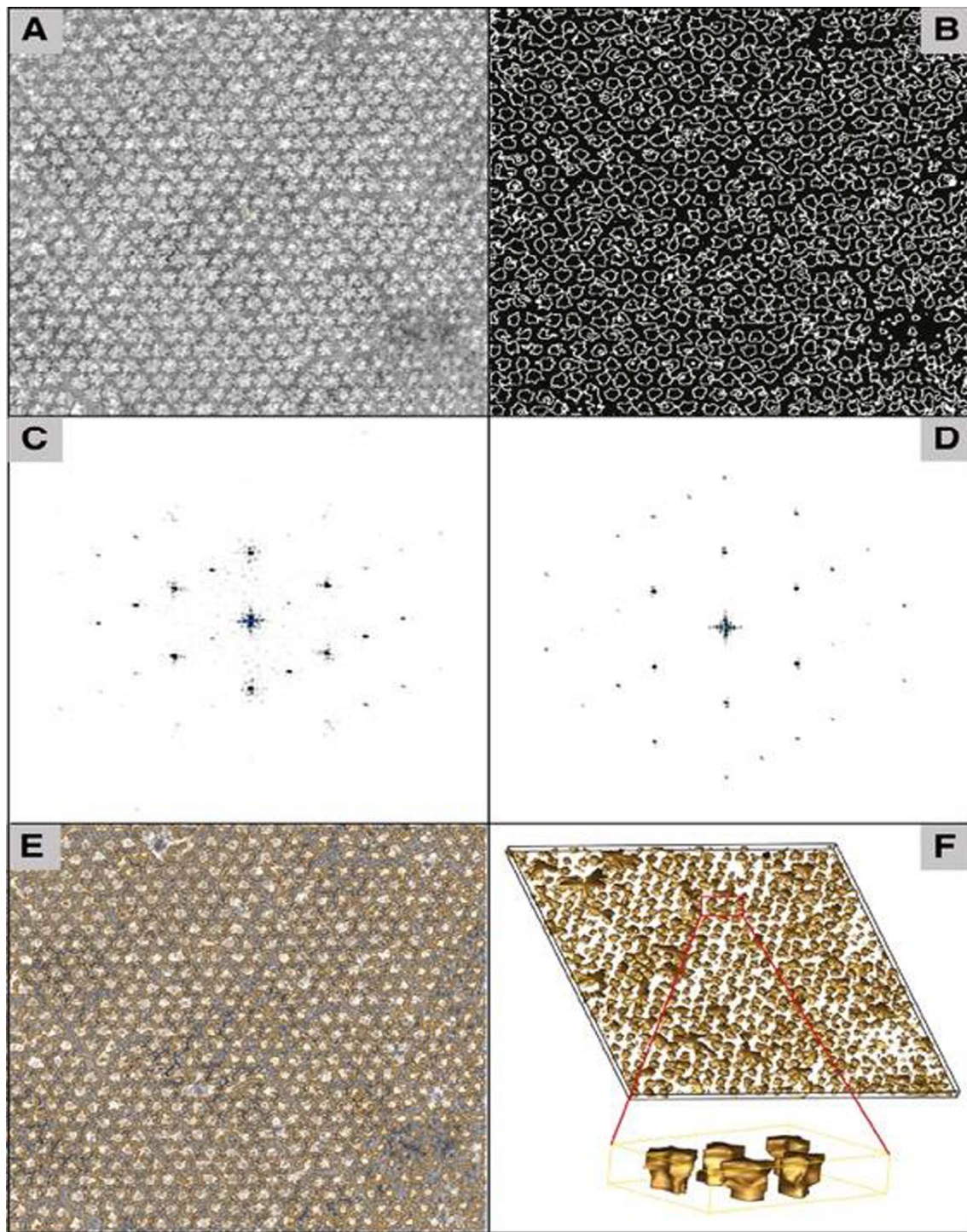
Fig. 6. Segmentation of V_0V_1 rotary ATPases through a 2D crystal. (A) 2D cross-section of a subvolume of a 2D crystalline array of T. thermophilus V_0V_1 rotary ATPase complexes (Gerle et al., 2006; Tani et al., 2013). (B) Application of RAZA outlining the edges of ATPase complexes shown in (A). (C) FFT of input slice shown in (A). (D) FFT of rendered tomogram shown in (B). (E) Contours shown in (B) overlaid on the 2D slice shown in (A). These contours/edges were detected using RAZA settings of z-crossings = 50 and σ = 0.49. (F) 3D surface rendered view of B showing the crowded organization of V-ATPase complexes within the ordered arrays.

Dataset 1 was a sub region of a whole cell tomogram recorded and reconstructed from images of a high-pressure frozen, freeze-substituted and plastic-embedded mouse pancreatic beta cell (Noske et al., 2008).

Dataset 2 was a tomographic volume reconstructed from images of the chloroplast region of a high pressure frozen, freeze-substituted, plastic-embedded *Chlamydomonas reinhardtii* cell (Ali et al., 2012).

Dataset 3 was a 3D reconstruction of vitrified mitochondria isolated from *Podospora anserina* and imaged by cryo-ET (Davies et al., 2011)

.
Dataset 4 was a 3D tomographic reconstruction of a 2D crystal of the V_0V_1 rotary ATPase isolated from *Thermus thermophilus* membranes (Tani et al., 2013).

Dataset 5 was a cryo-tomogram of *Bdellovibrio bacterivorous* HD100 cells of *E. coli,* prepared and imaged as described previously (Lambert and Sockett, 2005).

Dataset 6 was a tomogram of a high pressure frozen, freeze-substituted, resin-embedded pancreatic beta cell.
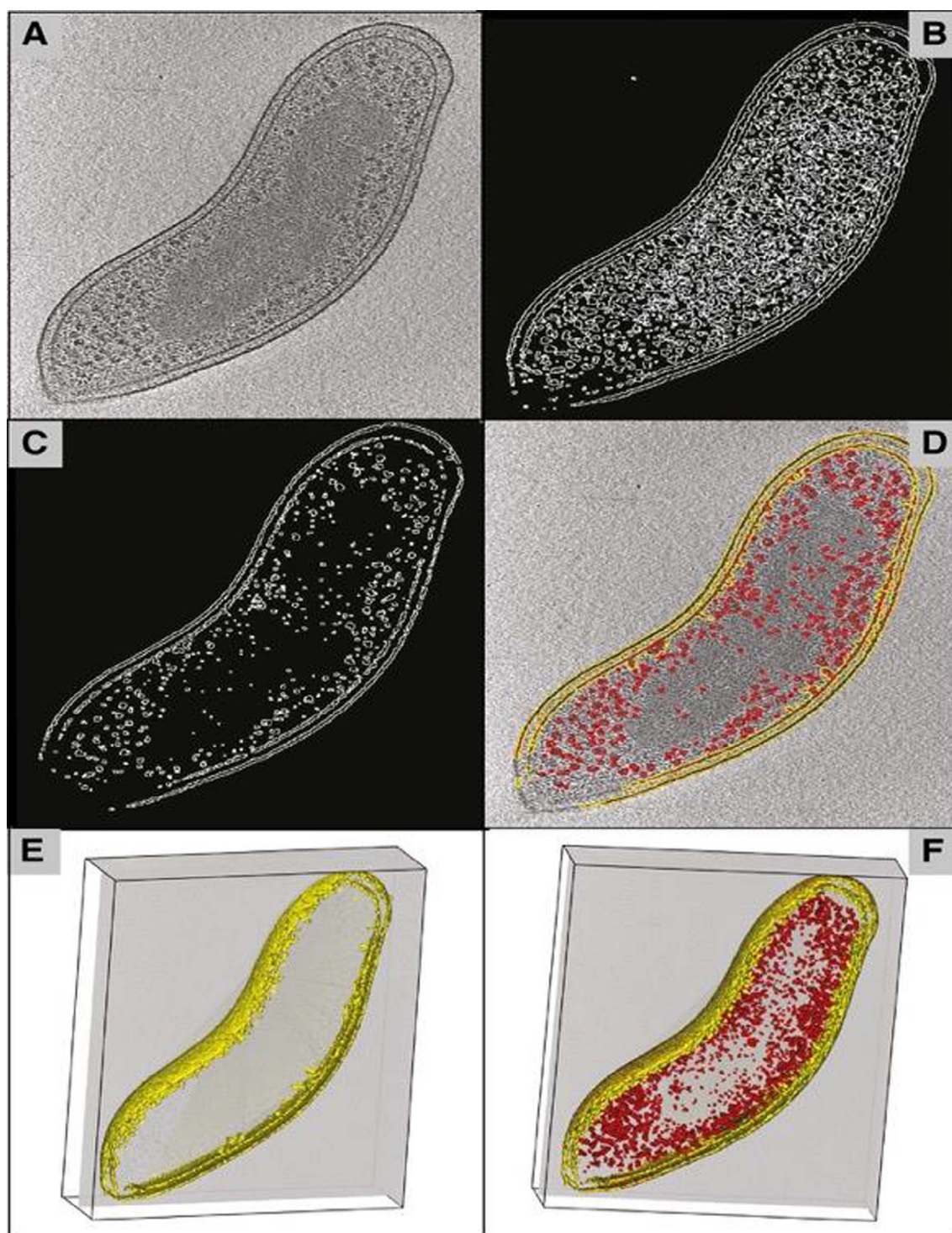
Fig. 7. Segmentation of membranes of *Bdellovibrio bacteriovorus* imaged under cryo conditions. (A) A 2D slice of a cryo-tomogram containing a membrane of B bacteriovorus HD100. (B) RAZA segmentation output using σ = 0.7 and z-crossings value = 378 optimized for membrane detection. (C) Application of RAZA using σ = 0.7 and z-crossings = 360 optimized for macromolecular structures. (D) Contours detected by RAZA with settings in B (in yellow) and C (in red) overlaid on the 2D tomographic view shown in A. (E) 3D surface view of cell membrane only. (F) Combined 3D surface view of membranes and macromolecules detected by RAZA using both parametric settings.

Dataset 7 was a serial section focused ion beam (FIB) dataset of *C. reinhardtii* cells.

4. Results and discussion

The segmentation process implemented in RAZA is summarized in Fig. 1. RAZA is applied to a small volume encompassing a single mitochondrion. In the raw tomogram (Fig. 1A) the outer mitochondrial

membranes (red arrow) and inner cristae (blue arrows) are clearly visible, as are other structural features surrounding the organelle.

Fig. 1B shows a single slice of the tomogram following Gaussian filtering and subsequent calculation of the first-order derivative *(rate of change of intensity)*. The *X* and *Y*-axes of Fig. 1B represent the X-Y tomogram axes while the *Z*-axis represents the range of first-order derivative values color-coded from blue (0) to red (2000). The highest first-order derivative values (i.e. the peaks uppermost in Fig. 1B) represent

voxels exhibiting the highest rate of intensity change; i.e. voxels centered around an edge. As pure first-order derivate filters do not discriminate between signal and noise, they lack the ability to accurately distinguish between *true* and *false* edges. This is evident from the large number of peaks observed. Fig. 1C demonstrates the Laplacian of Gaussian (LoG, i.e. second-order derivative of Gaussian) of a single slice through the tomogram shown in Fig. 1A. Again, the *X* and *Y*-axes correspond to those of the tomogram. Here however, the Z-axis indicates the second-order derivative values (*the rate of change of the gradient of intensity*) which show a more gradual (less noisy) change. The z-crossings values range from positive (red) to negative (blue). The zero crossing points are highlighted in yellow. It can be seen that positive (red) and negative (blue) z-crossings values correspond to the dark and light gray features in Fig. 1A respectively. The real space tomogram (Fig. 1D) has been rendered by tracing the zero crossings value calculated in Fig. 1C, to show edges representing the greatest rate of change in intensity. It can be seen that the application yields a segmented tomogram, which includes contours of the mitochondrial membrane and internal cristae, but also additional contours. Fig. 1D represents a 3D segmented objected after manually removing unwanted contours outside the mitochondrion region, shown in Fig. 1E. The amount of time required for manual removal of unwanted contours already represents a marked improvement compared to full manual segmentation of the tomogram and by using the 3D structural fingerprint parameters described below, the process can be speeded-up further.

To evaluate the performance of RAZA, we chose a diversity of datasets that reflect the wide range of conditions under which electron tomography data are routinely collected. These include a test volume populated with synthetic volumes and simulated noise (Supplementary Material I, Fig. S2, S3 and S6 and Table S1 and S3), as well as cellular tomograms populated with a variety of subcellular organelles (Fig. 2), an unstained vitrified tomogram containing membrane and membrane proteins (Fig. 3), a subcellular volume heavily populated with macromolecular assemblies (Fig. 4), A 2D membrane protein array, a sub-tomogram of a 2D crystalline array of *T. thermophilus* VoV1 rotary ATPase complexes (Fig. 6), and a vitrified tomographic section of membranes of *B. bacterivorous* (Fig. 7).

4.1. Segmentation of cellular tomography data

RAZA was tested using a more complex tomographic cellular subvolume acquired for a 300–400 nm thick section of a high-pressure frozen, freeze-substituted and plastic-embedded mouse islet pancreatic beta cell.

This tomographic volume contained a range of subcellular compartments differing in size, shape, orientation and gray scale values. The automated detection of such a wide range of objects remains challenging, limiting the ability to segment and annotate tomographic data in an automated manner. Fig. 2A shows a representative 2D slice through this volume. Following Gaussian smoothing (Fig. 2B), RAZA's Laplacian of Gaussian (LoG) filtration was applied (Fig. 2C) followed by extraction of the zero-crossing values. In Fig. 2D three object classes have been color coded in purple (mitochondria), yellow (mainly Golgi regions) and red (mainly mature insulin granules). Fig. 2E-I show a selection of edges detected in the slice from Fig. 2A by applying different z-crossings thresholds. Fig. 2E-I show the utility of RAZA's arbitrary z-crossing functionality (*the rate of change of the gradient of intensity*) over traditional zero-crossing (i.e. z = 0 which defines the maximum rate of change). In general, increasing σ minimizes noise; reducing σ preserves finer details but at the expense of increased noise contamination. The values used here were tuned to select the objects of interest. The yellow contours can be seen to define the small white subcellular structures (e.g. Golgi ribbon- Fig. 2G-H), while the purple (Fig. 2F) and red (Fig. 2I) contours delineated the light and dark gray objects in the image (e.g. mitochondria and mature insulin granules respectively).

For the purposes of annotation, analysis and selective representation it is important for biologists to have tools to extract specific objects. Fig. 2F–I show that through the selection of specific σ values and z-crossings thresholds, the white, gray and dark gray objects can be selectively visualized using IMOD functions (Kremer et al., 1996). These results demonstrate the capability of RAZA to conduct accurate, semi-automated segmentation of a wide range of subcellular volumes in resin-embedded samples, irrespective of their size, shape, volume, orientation and voxel intensity.

Having established that RAZA is capable of segmenting electron tomograms of biological samples accurately and in a semi-automated manner, studies were conducted to evaluate its performance (Fig. S4 C, D and F) in comparison with established manual segmentation approaches (Fig. S4 B and E). To compare the accuracy of RAZA-based and manual segmentation statistically, we quantified the surface areas and volumes obtained using both techniques (Table S2). RAZA output was found to be of a quality similar to that obtained using manual segmentation. Furthermore, RAZA was shown to perform well (Supplementary Material I, Fig. S6) against a range of well-established segmentation algorithms including the 3D Bilateral Edge filter (Ali et al., 2012), the 3D Recursive filter (Monga et al., 1991) and the 3D Canny filter (Canny, 1986).

4.2. Application of RAZA to cryo-tomography data

The segmentation of low contrast cryo-tomograms is substantially more challenging than the segmentation of higher contrast tomograms recorded on resin-embedded, heavy metal stained specimens. The performance of RAZA was therefore evaluated by comparing images of negatively stained (Fig. 3A, C and E) and vitrified mitochondria (Fig. 3B, D, F-H).

As can be seen in Fig. 3, contours defining the mitochondrial membranes are readily detected in both the higher contrast, negatively stained sample (Fig. 3E) as well as the much lower contrast cryo-tomogram (3F). The result of manual segmentation of the latter is presented in Fig. 3G, where the cristae membranes and several ATP synthase complexes, colored (ATP synthase dimers (yellow and red), the membrane (gray), complex I densities (green)) according to Davies et al. (2011) are clearly resolved. It should be noted that such segmentation requires expert knowledge, and is labour intensive, precluding high throughput analysis of this nature. Comparing the results obtained with RAZA, not only were the membranes effectively contoured, but protrusions corresponding to the location of ATP synthase molecules were also clearly seen (Fig. 3H). Smoothing of the ATPase complexes can be seen in RAZA-generated contours. This is explained by the fact that the settings were optimized for membrane detection rather than the detection of individual membrane proteins and because the electron density of the lipid bilayer and the transmembrane domains of the ATPase complexes are similar. This result demonstrates the capability of RAZA to conduct semi-automated segmentation of both membranes and large extracellular domains of membrane-embedded proteins. Although RAZA did not resolve protein contours within the transmembrane region of the mitochondrial membrane protein complexes in these images, the ability to localize membrane protein complexes of this size (via identification of their cytoplasmic domain) facilitates extraction and subsequent subvolume averaging using single particle tomography approaches.

4.3. Detecting macromolecular assemblies in electron tomograms

Having established that in terms of quality RAZA compares to best practice manual segmentation at the level of subcellular organelles and membranes, its ability to contour individual macromolecular assemblies using the structural finger print parameters was analyzed.

Fig. 4 shows the results obtained following the application of RAZA to a tomogram obtained for a cytoplasmic region of a high-pressure

frozen, freeze-substituted, resin-embedded *C. reinhardtii* cell (Ali et al., 2012). It contains 500 darkly-stained macromolecular assemblies equivalent to the size of ribosomes which were identified by manual curation. Using RAZA, contours defining the outline of these macromolecular assemblies were obtained (Fig. 4: A-C) thus demonstrating RAZA's ability to obtain 3D information defining the spatial arrangement of macromolecular assemblies in cells.

The ability to localize and rapidly segment a large number of individual macromolecular assemblies paves the way for the extraction of large 3D datasets for subsequent alignment, classification and molecular subvolume averaging. To refine the selection of macromolecular contours, 10 suitable 'reference' ribosome-like molecules were identified and based on these, average values were calculated for their 3D structural fingerprint parameters; the three axes, surface area and volume. This provides a comprehensive overview of the effect of adjusting individual and combinations of parameters between ± 0 and ± 100% of the threshold values. Under the most stringent conditions tested (all three axes, surface area to volume set to ± 20% of the reference values) only 14 particles (Fig. 4D) were selected. This indicates that one or more of these fingerprint variables for the undetected particles were outside of this threshold range. When only the three axes parameters were set ± 20% (Fig. 4E) the number of particles detected increased to 46 as the search was less stringently controlled (i.e. no restriction on surface area or volume). When conditions were relaxed further by setting the volume, surface area, major axis and minor axis (in separate tests) to ± 20% of the threshold values, the number of particles detected was 52, 56, 93 and 208 respectively (Fig. 4: F-I). This indicates that for this sample the minor axis was most variable. However, for all variables, increasing the threshold setting increased the number of particles detected (Fig. 5). Finally, when only the minor axis threshold was controlled and increased to 90%, 422 out of 500 black densities within the tomogram were detected (Fig. 4: J-L). The detection at 90% indicate that the structural parameters of darkly stained macromolecular assemblies vary by nearly twice the averaged dimensions of reference particles. This illustrates how an analyst can use the finger print parameters and their range settings to provide an extra level of control over particles selection by RAZA (Fig. 5).

A few much smaller black objects/noise spikes were detected at high threshold tolerance settings (95%) and these can be excluded through the choice of the active fingerprint variables and their threshold tolerance settings.

4.4. Segmentation of membrane protein complexes in a 2D crystal

Next we tested whether RAZA was able to faithfully reproduce lattice parameters of a 2D crystal grown from large membrane protein complexes.

A selected region of a tomographic volume obtained from a negatively stained *T. thermophilus* V-ATPase 2D crystal (Fig. 6A) showing an area of high coherence was extracted, and RAZA was applied with parametric settings of z-crossings = 50 and σ = 0.49 (Fig. 6B). RAZA accurately detected both the extrinsic and transmembrane regions of the V-ATPase (Fig. 6 E-F) in these reconstituted 2D crystals which lacked an intact lipid bilayer and were negatively stained. The accuracy of detection is supported by the comparison of z-slice Fourier transforms of the raw tomogram (Fig. 6C) and the segmented volume (Fig. 6D), where diffraction spots are seen beyond the first-order reflections and match that of the raw tomogram; if RAZA were segmenting noise, the reflections in Fig. 6D would be lost. This confirms that RAZA has accurately detected the ATPases in this 2D lattice.

4.5. Segmentation of a whole cell cryo tomogram

Having demonstrated that RAZA can segment organelles, membranes, extrinsic membrane protein domains in membranes and macromolecular assemblies under conditions that yielded sufficient contrast

to resolve their respective edges, its performance was next tested on cryo-tomograms of a whole cell. First the contours of the outer membrane of the *B. bacteriovorus* cells (Fig. 7A) were extracted.

In this process, the σ parameter determines and adjusts the width of LoG kernel (large σ more smoothing, useful for the segmentation of large objects; small σ useful to retain fine detail but more sensitive to noise), while manipulation of the z-crossings value improves the connectivity of true edge pixels. This can further be visualized by observing the intensity values obtained based on the second-order derivative (Supplementary material I, Fig. S2). In Fig. 7, the optimal σ value was found to be 0.7 for both membranes and membrane protrusions, as they both have similar widths. They did however have different optimal z-crossings values of 378 (Fig. 7B) and 360 (Fig. 7C), respectively. To select protrusions from the membranes more accurately a z-crossings value of 360 was used to eliminate false edges (Fig. 7C). Despite the low SNR and other artefacts of cryo-tomography (e.g. missing cone), RAZA recovered contours (Fig. 7E and F) close to those expected for the membrane.

4.6. Organellar fingerprinting: Selective mitochondrial identification

The next challenge was to establish whether the *structural fingerprinting* and the *selective thresholding* capability of RAZA could be used to automate the detection and segmentation of irregularly shaped objects such as mitochondria or other organelles in cellular tomograms. An experienced analyst can identify mitochondria by their shape, size and appearance. This suggests that appropriate pattern recognition algorithms should also be able to do so. But while macromolecules such as ribosomes are quite regular in size, the size, shape and structure of mitochondria can vary significantly.

Fig. 8A shows a slice of a 3D cell tomogram containing a range of different organelles, including mitochondria. When RAZA was applied to this data (Fig. 8B: z-crossings value = −5000 and σ = 3) all traced objects detected were mitochondria (i.e. no false positives), although not all mitochondria were detected (i.e. some false negatives). This suggests that the structural fingerprint threshold parameters had been defined too stringently in this case to accommodate the structural variability of mitochondria. The mitochondria not detected are indicted by the blue arrows in Fig. 8B. To improve mitochondrial detection, five reference mitochondria with a broad range of sizes were used as reference objects to calculate average search parameters for the three axis lengths (major, middle and minor), surface area and volume. Based on these values, thresholds were adjusted to include objects ± 20% of the average values for all five parameters. This approach, successfully detected 64 objects (Fig. 8C). More could be found by extending the parameters further. The complexity of these objects (gold) is best seen in Fig. 8C. The setting of the z-crossings value played an important role in defining the selection of mitochondria over other objects in the tomogram as it helped discriminate between objects with differing greyscale intensities. The use of a relatively large σ value (σ = 6) also proved to be beneficial, as it helped to suppress the detection of small objects which are smoothed out under these conditions. These results show that while mitochondria exhibit significant variability in size, shape and structure, RAZA was able to detect a significant subset of mitochondria within a complex cellular volume. This was achieved in a discriminative manner even with a low tolerance threshold of ± 20%. Closer analysis of this data suggests that mitochondrial identification was best achieved by the variables surface area, volume and minor axis. This provides useful insights into how skilled analysts successfully identify these objects.

5. Conclusion

The *Rapid z-crossings algorithm* (RAZA) is a high-throughput Laplacian-of-Gaussian edge-detector which can rapidly output discrete mathematically-defined object contours. RAZA can be configured to
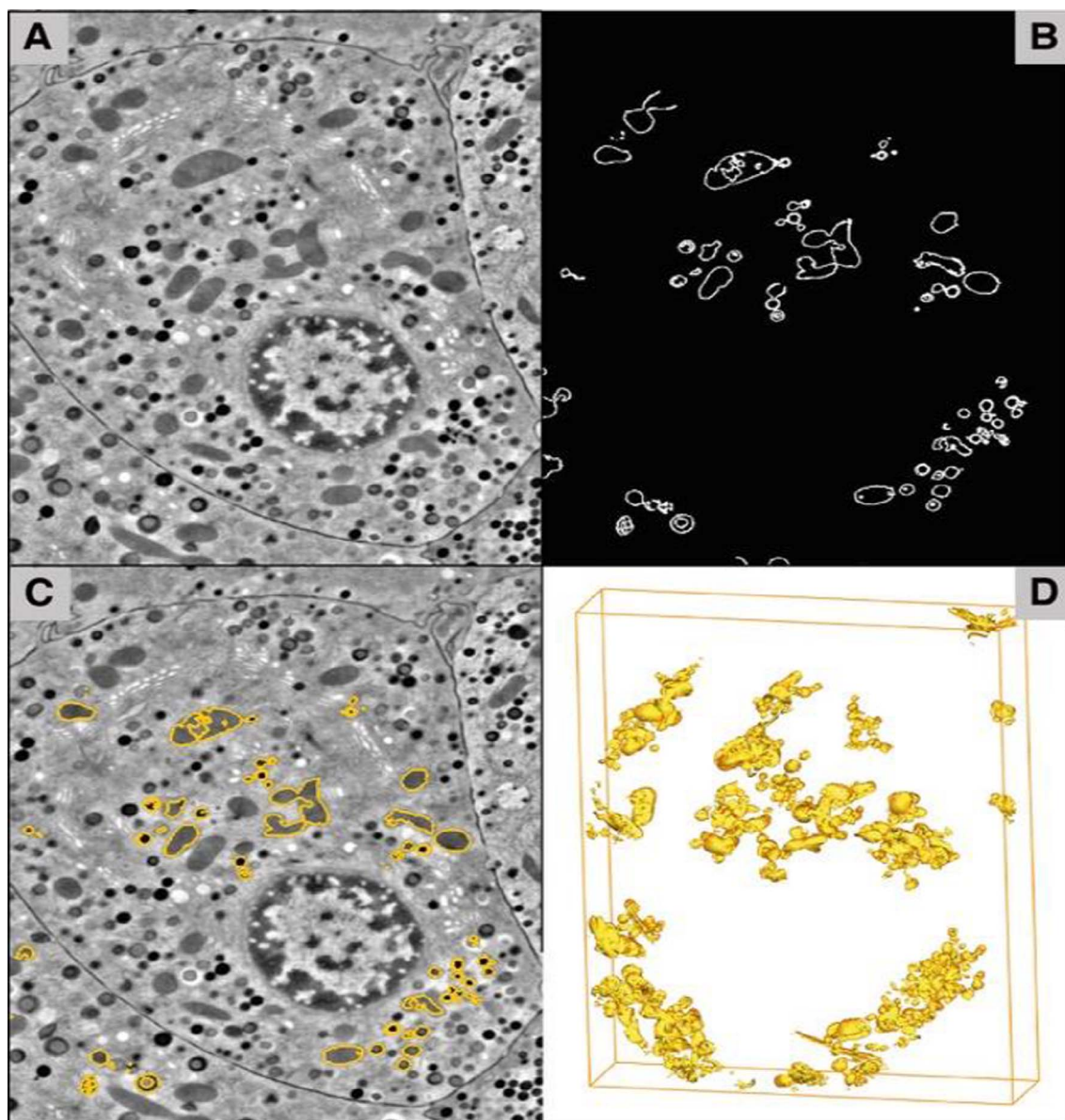
Fig. 8. RAZA based mitochondria detection. (A) Tomographic section of a high-pressure frozen, freeze-substituted and plastic-embedded mouse pancreatic beta cell. (B) Contours detected by RAZA using z-crossings value = −5000 and σ = 3. (C) 3D surface-rendered objects detected when the thresholds were set to 20% for all parameters (major, middle and minor axes, surface area and volume). (D). Contours overlaid on the original gray scale tomogram.

segment all detected objects within a tomogram, or a selected sub-population of objects (e.g. mitochondria or ribosomes), based on the z-crossings and σ values as well as the settings of object specific structural fingerprint parameters, which include the longest axis (*major axis*), a second longest axis orthogonal to this (*middle axis*) and the third orthogonal axis to these (*minor axis*) as well as the calculated surface area and volume of individual objects. Calculating these five parameters at the object level has the major advantage that it overcomes the problem of the 'random' orientation of subcellular structures (e.g. of ribosomes in cells).

These five structural fingerprint parameters were sufficient to selectively extract objects. For example, when searching for ribosomes, objects corresponding to organelles can largely be excluded through the use of any of the above structural finger print parameters as organelles are significantly larger in terms of their 3 axes, surface area and volume. In contrast, abundant macromolecular assemblies (e.g. ribosomes and proteasomes) are much more similar in their overall dimensions, and so all five parameters may be needed to distinguish between them. To segment specific subcellular structures (e.g. microtubules), their

selective detection could be assisted by searching for objects with a long major axis (corresponding to tubule length) and two smaller axes (corresponding to tubular cross section). In this scheme the major, middle and minor axes can be defined as object specific x, y and z axes. This is useful for subvolume averaging, as the axes can enable initial coarse alignment of the extracted particles (e.g. aligning objects along their longest axis). Thus, the axis parameters extracted by RAZA provide a reduced 'structure approximation' for each detected object. The 3D structural fingerprint of organelles can be used to identify them and to assess cell-wide differences in their morphology (Noske et al., 2008).

RAZA also calculates object centers, the location of which are defined as the intersection of the major, middle and minor axes. While there are alternative definitions of object centers (e.g. center of mass) the current definition is suitable for rapid high-throughput sub-volume extraction as it minimizes additional center calculation times and because precise centering is not essential for downstream sub-volume averaging. RAZA provides a bridge between the ever-increasing amount and quality of electron tomography data and the development of high throughput processes for sub-volume averaging, structural population

analysis and the development of atomic resolution 3D atlases of cells, by providing a framework that enables the subsequent molecular annotation and docking of atomic resolution protein models into the contours of macromolecular assemblies and membrane proteins in tomograms.

RAZA also offers significant potential for the construction of 'atomic resolution' 3D models of cells as the molecular contours of their constituent objects and their *structural fingerprints* provide a framework for semi-automated docking of atomic protein structures into cellular tomograms. With the current 'resolution revolution' in cryo-EM facilitated by advances in direct electron detectors (Kuhlbrandt, 2014), the number of atomic resolution membrane protein and macromolecule structures being solved is increasing rapidly. The high detective quantum efficiency of direct electron detectors (McMullan et al., 2014), particularly in single electron counting mode, may open up the opportunity not only to detect organelles and macromolecular assemblies, but to also routinely detect membrane proteins in membranes. Indeed, there are examples in the literature where membrane proteins have been visualized in isolated membranes (Kouril et al., 2012).

The rapidly expanding repository of atomic resolution X-ray structures of membrane proteins and macromolecular assemblies provides a ready source of molecular fingerprints in terms of their major, middle and minor axes, surface area and volume. In parallel RAZA can segment individual macromolecules in tomograms and extract both their structural fingerprints and centroid locations. As the quality of electron tomograms increases so will the ability to accurately match specifically contoured tomographic objects to specific atomic structures, based on the similarity of the structural fingerprints. Furthermore, because RAZA is able to define the centroid of each object as well as the major, middle and minor axes, irrespective of the orientation of the object within the cell. It can theoretically identify the location of specific objects in cells. Furthermore, RAZA can support the preliminary docking of atomic structures into high resolution electron tomograms. First the center of the segmented contour can be aligned to that of the macromolecular structures to be docked. Second, the max, *med* and min axes can be used to attain an approximate docking constraint prior to the use of more specialized docking refinement algorithms. Consequently, RAZA provides the basis for future docking of atomic resolution macromolecular structures into cellular tomograms.

Among the possible extensions of the work, the most interesting unsolved problem is the ability to resolve the transmembrane domains of membrane embedded proteins. This is expected to remain a limitation until imaging systems are improved to a point that molecular contours within the membrane plane can be detected. Additionally, the output of RAZA is binary. However, to color the objects selectively, many other tools are available and have been used effectively. Although the guidance to optimize parameters (σ and z-crossings value) intelligently is provided, user based starting parameter selection is still required.

Author contribution

R.A.A. A.M.M and C.G performed research. R.A.A., M.J.L and B.H designed research. R.A.A., A.M.M., M.J.L N.A.H and B.H analyzed data. R.A.A and R.R performed experiment. R.A.A, M.J.L, and B.H. wrote the paper. All authors reviewed the manuscript.

Acknowledgement

Appendix A. Supplementary data

Supplementary data associated with this article can be found, in the online version, at http://dx.doi.org/10.1016/j.jsb.2017.10.002.

References

Adiga, P.S., Malladi, R., Baxter, W., Glaeser, R.M., 2004. A binary segmentation approach for boxing ribosome particles in cryo EM micrographs. J. Struct. Biol. 145, 142–151.

Alber, F., Forster, F., Korkin, D., Topf, M., Sali, A., 2008. Integrating diverse data for structure determination of macromolecular assemblies. Annu. Rev. Biochem. 77, 443–477.

Ali, R.A., 2016. Developing 3D novel edge detection and particle picking tools for electron tomography (Ph.D thesis). The University of Queensland, Australia.

Ali, R.A., Landsberg, M.J., Knauth, E., Morgan, G.P., Marsh, B.J., Hankamer, B., 2012. A 3D image filter for parameter-free segmentation of macromolecular structures from electron tomograms. PLoS One 7, e33697.

Asano, S., Fukuda, Y., Beck, F., Aufderheide, A., Forster, F., Danev, R., Baumeister, W., 2015. Proteasomes. A molecular census of 26S proteasomes in intact neurons. Science 347, 439–442.

Bajaj, C., Yu, Z., Auer, M., 2003. Volumetric feature extraction and visualization of tomographic molecular imaging. J. Struct. Biol. 144, 132–143.

Baker, M.L., Yu, Z., Chiu, W., Bajaj, C., 2006. Automated segmentation of molecular subunits in electron cryomicroscopy density maps. J. Struct. Biol. 156, 432–441.

Canny, J., 1986. A computational approach to Edge detection. IEEE Trans. Pattern Anal. Mach. Intell. PAMI-8 679–698.

Cardenes, R., Zhang, C., Klementieva, O., Werner, S., Guttmann, P., Pratsch, C., Cladera, J., Bijnens, B.H., 2017. 3D membrane segmentation and quantification of intact thick cells using cryo soft X-ray transmission microscopy: A pilot study. Plos One 12.

Castano-Diez, D., Kudryashev, M., Arheit, M., Stahlberg, H., 2012. Dynamo: a flexible, user-friendly development tool for subtomogram averaging of cryo-EM data in high-performance computing environments. J. Struct. Biol. 178, 139–151.

Comolli, L.R., Baker, B.J., Downing, K.H., Siegerist, C.E., Banfield, J.F., 2009. Three-dimensional analysis of the structure and ecology of a novel, ultra-small archaeon. ISME J. 3, 159–167.

Danev, R., Buijsse, B., Khoshouei, M., Plitzko, J.M., Baumeister, W., 2014. Volta potential phase plate for in-focus phase contrast transmission electron microscopy. Proc. Natl. Acad. Sci. U.S.A. 111, 15635–15640.

Daum, B., Nicastro, D., Austin 2nd, J., McIntosh, J.R., Kuhlbrandt, W., 2010. Arrangement of photosystem II and ATP synthase in chloroplast membranes of spinach and pea. Plant Cell 22, 1299–1312.

Davies, K.M., Strauss, M., Daum, B., Kief, J.H., Osiewacz, H.D., Rycovska, A., Zickermann, V., Kuhlbrandt, W., 2011. Macromolecular organization of ATP synthase and complex I in whole mitochondria. Proc. Natl. Acad. Sci. U.S.A. 108, 14121–14126.

Engel, B.D., Schaffer, M., Kuhn Cuellar, L., Villa, E., Plitzko, J.M., Baumeister, W., 2015. Native architecture of the Chlamydomonas chloroplast revealed by in situ cryo-electron tomography. Elife 4.

Fernandez, J.J., 2009. TOMOBFLOW: feature-preserving noise filtering for electron tomography. BMC Bioinf. 10, 178.

Fernandez, J.J., Carrascosa, J.L., 2010. Image processing in electron tomography. Microscopy Science, Technology, Application and Education.

Fernandez, J.J., Luque, D., Caston, J.R., Carrascosa, J.L., 2008. Sharpening high resolution information in single particle electron cryomicroscopy. J. Struct. Biol. 164, 170–175.

Frangakis, A.S., Bohm, J., Forster, F., Nickell, S., Nicastro, D., Typke, D., Hegerl, R., Baumeister, W., 2002. Identification of macromolecular complexes in cryoelectron tomograms of phantom cells. Proc. Natl. Acad. Sci. U.S.A. 99, 14153–14158.

Galaz-Montoya, J.G., Flanagan, J., Schmid, M.F., Ludtke, S.J., 2015. Single particle tomography in EMAN2. J. Struct. Biol. 190, 279–290.

Garduno, E., Wong-Barnum, M., Volkmann, N., Ellisman, M.H., 2008. Segmentation of electron tomographic data sets using fuzzy set theory principles. J. Struct. Biol. 162,

368–379.

Gerle, C., Tani, K., Yokoyama, K., Tamakoshi, M., Yoshida, M., Fujiyoshi, Y., Mitsuoka, K., 2006. Two-dimensional crystallization and analysis of projection images of intact Thermus thermophilus V-ATPase. J. Struct. Biol. 153, 200–206.

Gonzalez, R.C., 2002a. Digital Image Processing. Prentice Hall, New Jersey.

Hrabe, T., Chen, Y., Pfeffer, S., Cuellar, L.K., Mangold, A.V., Forster, F., 2012. PyTom: a python-based toolbox for localization of macromolecules in cryo-electron tomograms and subtomogram analysis. J. Struct. Biol. 178, 177–188.

Jiang, W., Baker, M.L., Wu, Q., Bajaj, C., Chiu, W., 2003. Applications of a bilateral de-noising filter in biological electron microscopy. J Struct Biol 144, 114–122.

John, C., 1986. A computational approach to edge detection. IEEE Trans.: Pattern Anal. Mach. Intell. PAMI-8 679–698.

Prewitt, Judith M.S., 1970. Object Enhancement and Extraction. Picture processing and Psychopictorics. Academic Press.

Kang, S., Lee, C.Y., Goncalves, M., Chisholm, A.D., Cosman, P.C., 2015. Tracking epi-thelial cell junctions in C. elegans embryogenesis with active contours guided by SIFT flow. IEEE Trans. Biomed. Eng. 62, 1020–1033.

Kass, M., Witkin, A., Terzopoulos, D., 1988. Snakes: active contour models. Int. J. Comput. Vision 321–331.

Kizilyaprak, C., Longo, G., Daraspe, J., Humbel, B.M., 2015. Investigation of resins sui-table for the preparation of biological sample for 3-D electron microscopy. J. Struct. Biol. 189, 135–146.

Kouril, R., Dekker, J.P., Boekema, E.J., 2012. Supramolecular organization of photo-system II in green plants. Biochim. Biophys. Acta 1817, 2–12.

Kremer, J.R., Mastronarde, D.N., McIntosh, J.R., 1996. Computer visualization of three-dimensional image data using IMOD. J. Struct. Biol. 116, 71–76.

Kuhlbrandt, W., 2014. Cryo-EM enters a new era. Elife 3, e03678.

Lambert, C., Sockett, R.E., 2005. Laboratory Maintenance of Bdellovibrio, Current Protocols in Microbiology. John Wiley & Sons Inc.

Lebbink, M.N., Geerts, W.J.C., van der Krift, T.P., Bouwhuis, M., Hertzberger, L.O., Verkleij, A.J., Koster, A.J., 2007. Template matching as a tool for annotation of to-mograms of stained biological structures. J. Struct. Biol. 158, 327–335.

Luengo, I., Darrow, M.C., Spink, M.C., Sun, Y., Dai, W., He, C.Y., Chiu, W., Pridmore, T., Ashton, A.W., Duke, E.M.H., Basham, M., French, A.P., 2017. SuRVoS: super-region volume segmentation workbench. J. Struct. Biol. 198, 43–53.

Mallick, S.P., Zhu, Y., Kriegman, D., 2004. Detecting particles in cryo-EM micrographs using learned features. J. Struct. Biol. 145, 52–62.

Marr, D., Hildreth, E., 1980. Theory of edge detection. Proc. R. Soc. London. Ser. B. Biol. Sci. 207, 187–217.

Martinez-Sanchez, A., Garcia, I., Fernandez, J.J., 2011. A differential structure approach to membrane segmentation in electron tomography. J. Struct. Biol. 175, 372–383.

Martinez-Sanchez, A., Garcia, I., Asano, S., Lucic, V., Fernandez, J.J., 2014. Robust membrane detection based on tensor voting for electron tomography. J. Struct. Biol. 186, 49–61.

McMullan, G., Faruqi, A.R., Clare, D., Henderson, R., 2014. Comparison of optimal per-formance at 300 keV of three direct electron detectors for use in low dose electron microscopy. Ultramicroscopy 147, 156–163.

Monga, O., Deriche, R., Malandain, G., Cocquerez, J.P., 1991. Recursive filtering and edge tracking: two primary tools for 3D edge detection. Image Vision Comput. 9, 203–214.

Moussavi, F., Heitz, G., Amat, F., Comolli, L.R., Koller, D., Horowitz, M., 2010. 3D seg-mentation of cell boundaries from whole cell cryogenic electron tomography vo-lumes. J. Struct. Biol. 170, 134–145.

Nicastro, D., Schwartz, C., Pierson, J., Gaudette, R., Porter, M.E., McIntosh, J.R., 2006. The molecular architecture of axonemes revealed by cryoelectron tomography. Science 313, 944–948.

Noske, A.B., Costin, A.J., Morgan, G.P., Marsh, B.J., 2008. Expedited approaches to whole cell electron tomography and organelle mark-up in situ in high-pressure frozen pancreatic islets. J. Struct. Biol. 161, 298–313.

Pantelic, R.S., Ericksson, G., Hamilton, N., Hankamer, B., 2007. Bilateral edge filter: photometrically weighted, discontinuity based edge detection. J. Struct. Biol. 160, 93–102.

Pantelic, R.S., Fu, W., Schoenenberger, C., Stahlberg, H., 2014. Rendering graphene supports hydrophilic with non-covalent aromatic functionalization for transmission electron microscopy. Appl. Phys. Lett. 104, 134103.

Pantelic, R.S., Rothnagel, R., Huang, C.Y., Muller, D., Woolford, D., Landsberg, M.J., McDowall, A., Pailthorpe, B., Young, P.R., Banks, J., Hankamer, B., Ericksson, G., 2006. The discriminative bilateral filter: an enhanced denoising filter for electron microscopy data. J. Struct. Biol. 155, 395–408.

Rafael, C., Gonzalez, R.E.W., 2002b. Digital Image Processing, second ed. Prentice-Hall.

Ramachandra, R., Bouwer, J.C., Mackey, M.R., Bushong, E., Peltier, S.T., Xuong, N.H., Ellisman, M.H., 2014. Improving signal to noise in labeled biological specimens using energy-filtered TEM of sections with a drift correction strategy and a direct detection device. Microsc. Microanal. 20, 706–714.

Reichel, J., Menegaz, G., Nadenau, M.J., Kunt, M., 2001. Integer wavelet transform for embedded lossy to lossless image compression. IEEE Trans. Image Process. 10, 383–392.

Roberts, L.G., 1963. Machine Perception of Three-dimensional Soups. Massachusetts Institute of Technology.

Roerdink, J., Meijster, A., 2001. The watershed transform: definations, algorithms and parallelization strategies. Fundamenta Informaticae 41, 187–228.

Sandberg, K., 2007. Methods for image segmentation in cellular tomography. Methods Cell Biol. 79, 769–798.

Shapiro, L.G., Linda, G., Stockman, George C., 2002. Computer Vision. Prentice Hall.

Sijbers, J., Scheunders, P., Verhoye, M., van der Linden, A., van Dyck, D., Raman, E., 1997. Watershed-based segmentation of 3D MR data for volume quantization. Magn. Reson. Imaging 15, 679–688.

Starborg, T., Kalson, N.S., Lu, Y.H., Mironov, A., Cootes, T.F., Holmes, D.F., Kadler, K.E., 2013. Using transmission electron microscopy and 3View to determine collagen fibril size and three-dimensional organization. Nat. Protoc. 8, 1433–1448.

Tani, K., Arthur, C.P., Tamakoshi, M., Yokoyama, K., Mitsuoka, K., Fujiyoshi, Y., Gerle, C., 2013. Visualization of two distinct states of disassembly in the bacterial V-ATPase from Thermus thermophilus. Microscopy 62, 467–474.

Tomasi, C., Manduchi, R., 1998. Bilateral filtering for gray and color images. In: Sixth International Conference on. IEEE, 839-846.

van der Heide, P., Xu, X.P., Marsh, B.J., Hanein, D., Volkmann, N., 2007. Efficient au-tomatic noise reduction of electron tomographic reconstructions based on iterative median filtering. J. Struct. Biol. 158, 196–204.

Villa, E., Schaffer, M., Plitzko, J.M., Baumeister, W., 2013. Opening windows into the cell: focused-ion-beam milling for cryo-electron tomography. Curr. Opin. Struct. Biol. 23, 771–777.

Volkmann, N., 2010. Methods for segmentation and interpretation of electron tomo-graphic reconstructions. Methods Enzymol. 483, 31–46.

Woolford, D., Hankamer, B., Ericksson, G., 2007. The Laplacian of Gaussian and arbitrary z-crossings approach applied to automated single particle reconstruction. J. Struct. Biol. 159, 122–134.

Yamashita, E., Zhang, H., Cramer, W.A., 2007. Structure of the cytochrome b6f complex: quinone analogue inhibitors as ligands of heme cn. J. Mol. Biol. 370, 39–52.

Yu, Z.Y., Bajaj, C., 2005. Automatic ultrastructure segmentation of reconstructed CryoEM maps of icosahedral viruses. IEEE Trans. Image Process. 14, 1324–1337.

Yu, Z.Y., Holst, M.J., Hayashi, T., Bajaj, C.L., Ellisman, M.H., McCammon, J.A., Hoshijima, M., 2008. Three-dimensional geometric modeling of membrane-bound organelles in ventricular myocytes: bridging the gap between microscopic imaging and mathematical simulation. J. Struct. Biol. 164, 304–313.

Zhu, Y., Carragher, B., Mouche, F., Potter, C.S., 2003. Automatic particle detection through efficient Hough transforms. IEEE Trans. Med. Imaging 22, 1053–1062.